THREE-COLOR HEXAGONAL FINITE VOLUME METHODS WITH APPLICATION TO POISSON EQUATION AND ELECTRICAL WAVE PROPAGATION IN CARDIAC TISSUE

DANIEL LEE* AND HUI-CHUN TIEN†

Abstract. We consider in this work hexagonal finite volume methods for two-dimensional applications. Ordinary and compact seven-point schemes with three-color iterative updates are investigated with application to elliptic equations and reaction-diffusion systems. In particular, electrical activity of human ventricular tissue is observed. Monodomain model for human ventricular cell is used to simulate action membrane potential, and electrical wave propogation acrossing two dimensional myocardiac tissue can be obtained. The results have shown good agreement with previous research works.

Key Words: Hexagonal finite volume, Monodomain model, Multicolor ordering update.

AMS Subject Classification: 65-05, 65M06

1. Introduction. In a recent study of the origin of U-wave in ECG (electrocardiogram) [2], hexagonal subregions are adopted in numerical simulation of human heart electrophysiology. However, it was a pure algebraic approach in obtaining the ECG phenomena. Actually, cardiac electrical activity can be described by a system of reaction-diffusion equations and we refer to [3] for general references. Numerical simulation of cardiac electrophysiology can provide detailed observations for electrical activities of the heart. It is also a useful tool for understanding the mechanism of heart rhythm dynamics.

We consider in this study the hexagonal FV (finite volume) scheme with three-color iterative updates and its validation on elliptic equations and reaction-diffusion systems. Also, we investigate its application to the study of cardiac electrophysiology. In our work, a realistic human ventricular cell model developed by ten Tusscher et.al [14] is adopted. This model has incorporated recent experimental data from human myocardium and is capable of reproducing experimentally observed results, such as major ionic currents, action potential duration resitution and heart arrhythmias. In this work, the monodomain model is used and solved efficiently by three-color hexagonal FV method to simulate the eletrical activity of ventricular tissue. Linear electrical wave propagation on a two-dimensional cardiac tissue has been successfully observed and show satisfactory consistency with literature results.

Note that the slice of human ventricular tissue can be approximated by an ellipsoid of revolution. Hexagonal FVs are more flexible and relatively easy to construct for such irregular geometric region, thus yielding significant reduction in computational complexity.

As for the remaining sections, the concept and notations of a regular hexagon in general configuration are introduced in Section 2. Hexagonal FVM (finite volume method) in solving Poisson equation is discussed in Section 3, in which an ordinary seven-point scheme is obtained. This leads to a compact scheme with application to solving differential equations in Section 4. Numerical experiments and observations are given in Section 5, and conclusions drawn in the final section. In appendices, we highlight some theories for ease of reference and present a conventional FD approach to the special case of type II hexagons.

2. Preliminaries. In two-dimensional applications of configurations consisting of cartesian type (regular) hexagons, we denote by r the radius of hexagons and $h(=\frac{\sqrt{3}}{2}r)$ half of

[1]Department of Applied mathematics, Tunghai University, Taichung 40704,Taiwan (danlee@thu.edu.tw).
[2]Department of Financial and Computational Mathematics, Providence University, Taichung 40704,Taiwan (hctien@pu.edu.tw).

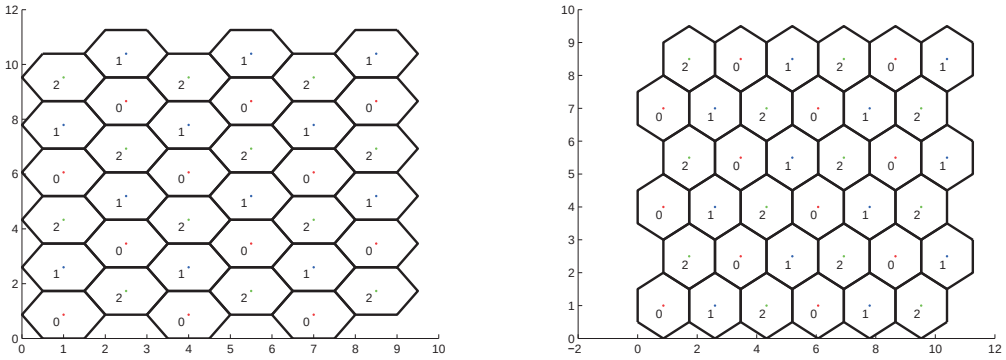

(a) Type I, phase angle $\varphi = 0$.

(b) Type II, phase angle $\varphi = -\frac{\pi}{6}$.

FIG. 2.1. *Hexagonal finite volumes in three colors.*

the *center-to-center* distance. The area of a hexagon is $|\Omega| = \frac{3\sqrt{3}}{2}r^2 = 2\sqrt{3}h^2$. Based on two configurations as indicated in Fig.2.1, coordinates of centers are given in Tables 2.1-2.2 and are indexed as for a cartesian mesh. The centers are in three different colors as to enable a three-color iterative method, that we will discuss in Section 4.4.

TABLE 2.1
Net of hexagons in configuration type I.

Phase angle : $\varphi = 0$		
Center point	i^{even}	i^{odd}
$cx(i,j)$	$(1.5i - 0.5)r$	
$cy(i,j)$	$2jh$	$(2j-1)h$

TABLE 2.2
Net of hexagons in configuration type II.

Phase angle : $\varphi = -\frac{\pi}{6}$		
Center point	j^{even}	j^{odd}
$cx(i,j)$	$2ih$	$(2i-1)h$
$cy(i,j)$	$(1.5j - 0.5)r$	

Our goal is to investigate hexagonal FVM and apply the technique to solve elliptic and parabolic type partial differential equations.

For a hexagon Ω in general configuration with phase angle φ, we consider the center node $P_0 = (x_0, y_0)$, its associated vertices,

$$V_k = (x_k, y_k) = (x_0, y_0) + r(\cos\theta_k, \sin\theta_k),$$

and neighbor centers,

$$P_k = (x_0, y_0) + 2h\big(\cos(\theta_k + \frac{\pi}{6}), \sin(\theta_k + \frac{\pi}{6})\big),$$

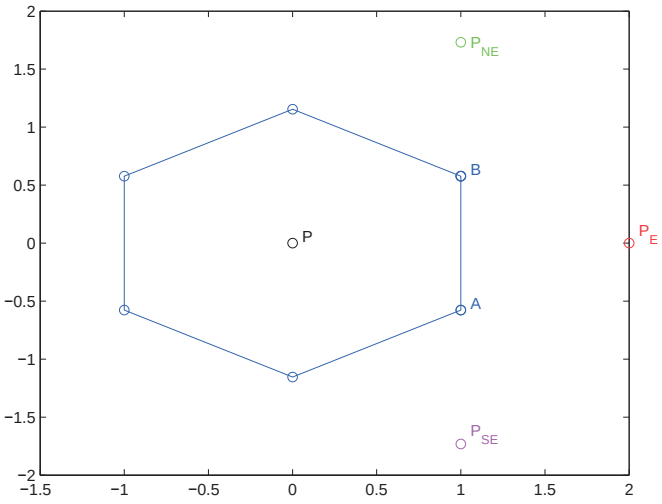

FIG. 3.1. *Boundary integral on edges of a type II hexagon.*

with $\theta_k = \varphi + \frac{k\pi}{3},\ k = 1, \cdots, 6$. We assume that $V_{6+k} = V_k$ periodically extended for convenience.

3. Hexagonal Finite Volume Method. We consider Poisson equation, $\nabla(k\nabla u) = f$, and apply FVM [15] to its integral formulation on a hexagon Ω,

$$\frac{1}{|\Omega|}\iint_{\Omega} div(k\nabla u)dxdy = \frac{1}{|\Omega|}\iint_{\Omega} f dxdy. \tag{3.1}$$

Discretization of the left-hand side is discussed below, while the right-hand side is discretized in various ways in Section 4.

3.1. Mid-point rule. We assume unit constant diffusivity for simplicity and note that

$$\begin{aligned} \tfrac{1}{|\Omega|}\iint_{\Omega} div(k\nabla u)dxdy = \quad & \tfrac{1}{|\Omega|}\int_{\partial\Omega} k\tfrac{\partial u}{\partial \vec{n}} d\gamma(t) && \approx \tfrac{1}{|\Omega|}\sum_{i=1}^{6}\left(k\tfrac{\partial u}{\partial \vec{n}}(m_i)\right)|\Delta\gamma_i| \\ \approx \quad & \tfrac{1}{2\sqrt{3}h^2}\sum_{i=1}^{6}\tfrac{u(P_i)-u(P_0)}{\sqrt{3}r} r && = \tfrac{1}{6h^2}\sum_{i=1}^{6}(u(P_i)-u(P_0)), \end{aligned} \tag{3.2}$$

where $|\Delta\gamma_i|$ denotes the length of the i-th boundary edge and m_i the mid-point of that edge. The boundary integral is thus approximated by a discrete seven-point stencil. We investigate below alternative views of numerical approximations to the path-integral.

3.2. Trapezoid rule. Up to rotation, we refer our argument to the configuration indicated in Fig.3.1, in which P, $P_{_E}$, $P_{_{SE}}$, $P_{_{NE}}$ denotes the cell center, the east neighbor (center) node, the south-east neighbor node and the north-east neighbor node, respectively.

Let $\overrightarrow{AB}$ be a positively oriented directed edge on the boundary, we consider at the end point A the truncated Taylor expansion in the normal-tangent coordinates $(\vec{n}, \vec{T})$. Explicitly, the local coordinates are

$$\begin{array}{rcccl} P-A & = & r(\cos\frac{5\pi}{6},\sin\frac{5\pi}{6}) & = & (-\frac{\sqrt{3}r}{2},\frac{r}{2})\,, \\ P_{_E}-A & = & r(\cos\frac{\pi}{6},\sin\frac{\pi}{6}) & = & (\frac{\sqrt{3}r}{2},\frac{r}{2})\,, \\ P_{_{SE}}-A & = & r(\cos\frac{-\pi}{2},\sin\frac{-\pi}{2}) & = & (0,-r)\,. \end{array}$$

The truncated Taylor expansion yields

$$\begin{bmatrix} 1 & \frac{-\sqrt{3}r}{2} & \frac{r}{2} \\ 1 & \frac{\sqrt{3}r}{2} & \frac{r}{2} \\ 1 & 0 & -r \end{bmatrix} \begin{pmatrix} u(A) \\ \partial_n u(A) \\ \partial_{_T} u(A) \end{pmatrix} = \begin{pmatrix} u(P) \\ u(P_{_E}) \\ u(P_{_{SE}}) \end{pmatrix},$$

which implies, among other things,

$$\partial_n u(A) = \frac{u(P_{_E})-u(P)}{\sqrt{3}r} = \frac{u(P_{_E})-u(P)}{2h}\,.$$

Similarly, at the endpoint B,

$$\begin{array}{rcccl} P-B & = & r(\cos\frac{-5\pi}{6},\sin\frac{-5\pi}{6}) & = & (-\frac{\sqrt{3}r}{2},-\frac{r}{2})\,, \\ P_{_E}-B & = & r(\cos\frac{-\pi}{6},\sin\frac{-\pi}{6}) & = & (\frac{\sqrt{3}r}{2},-\frac{r}{2})\,, \\ P_{_{NE}}-B & = & r(\cos\frac{\pi}{2},\sin\frac{\pi}{2}) & = & (0,r)\,, \end{array}$$

and

$$\begin{bmatrix} 1 & \frac{-\sqrt{3}r}{2} & \frac{-r}{2} \\ 1 & \frac{\sqrt{3}r}{2} & \frac{-r}{2} \\ 1 & 0 & r \end{bmatrix} \begin{pmatrix} u(B) \\ \partial_n u(B) \\ \partial_{_T} u(B) \end{pmatrix} = \begin{pmatrix} u(P) \\ u(P_{_E}) \\ u(P_{_{NE}}) \end{pmatrix}.$$

We obtain the same identical expression for approximated normal flux

$$\partial_n u(B) = \frac{u(P_{_E})-u(P)}{\sqrt{3}r} = \frac{u(P_{_E})-u(P)}{2h}\,.$$

Thus the trapezoid rule is identical to the mid-point rule in current application.

3.3. Simpson's rule. Usually, the Simpson's rule can be derived as a *nontrivial* convex combination of mid-point and trapezoid rules so as to eliminate the leading (second-order) error term and result in a fourth-order scheme in the presence of symmetry in the error expansion. This idea is not applicable in current situation. However, to derive a possible Simpson's rule for the line integrals, we try

$$\partial_n u(m_i) := \frac{u(P_i)-u(P)}{\sqrt{3}r}, \quad \partial_n u(V_i) := \frac{\partial_n u(m_i)+\partial_n u(m_{i-1})}{2}, \quad i=1,...,6.$$

Applied to the three points, $V_i(\equiv A), V_{i+1}(\equiv B)$ and $m_i(\equiv \frac{V_i+V_{i+1}}{2})$, Simpson's rule reads

$$\begin{aligned} \sum_{i=1}^{6} \int\limits_{\overline{V_i V_{i+1}}} (\partial_n u)\, d\gamma &\approx \sum_{i=1}^{6} r\frac{\partial_n u(V_i)+4\,\partial_n u(m_i)+\partial_n u(V_{i+1})}{6} \\ &= r\sum_{i=1}^{6} \frac{\partial_n u(m_{i-1})+10\,\partial_n u(m_i)+\partial_n u(m_{i+1})}{12} = r\sum_{i=1}^{6}\partial_n u(m_i). \end{aligned}$$

Thus yields the same expression as the mid-point rule.

Now these three discretization schemes are identical for the flux integral. The order of *the above* Simpson's rule remains two, locally on each edge of a hexagon. Actually, the accuracy of the estimated value of $\partial_n u(m_i)$ is of second-order only. One should not expect a fourth-order scheme. It turns out a surprise that the mid-point rule, obviously just a local second-order approximation to each line integral, achieves the same order of global accuracy (Theorem A.2) for the whole boundary and domain integral, due to the symmetry of global geometry. We refer to [6] for a general proof. Given below is an argument for special cases of type I and II hexagons.

THEOREM 3.1. *(H7 - Ordinary seven-point scheme.) Assume $u(x, y)$ is sufficiently smooth, then*

$$\frac{1}{|\Omega|}\iint_{\Omega} \triangle u \, dxdy = \frac{1}{6h^2}\sum_{j=1}^{6}(u(P_j) - u(P_0)) + \mathcal{O}(h^2).$$

Proof. We show the discretization is exact for low degree shifted monomial test functions, $u = (x - x_0)^m (y - y_0)^n,\ 0 \le m, n \le 2$. The case $m = n = 0$ $(u = 1)$ is trivial. For the other five cases, $(m, n) \in \{(1, 0), (0, 1), (2, 0), (0, 2), (1, 1)\}$, we claim

$$\tfrac{1}{|\Omega|}\iint_{\Omega} \triangle \left((x - x_0)^m (y - y_0)^n\right) \, dxdy = \tfrac{1}{6h^2}\sum_{j=1}^{6} \cos^m(\varphi + \tfrac{j\pi}{3}) \sin^n(\varphi + \tfrac{j\pi}{3}).$$

Indeed, the LHS values are respectively, $\{0, 0, 2, 2, 0\}$, by *symmetry* of the hexagon. For the RHS, elementary argument applies,

$$\begin{aligned}
&m = 1, n = 0, && \textstyle\sum_{j=1}^{6} \cos(\varphi + \frac{j\pi}{3}) && = 0,\\
&m = 0, n = 1, && \textstyle\sum_{j=1}^{6} \sin(\varphi + \frac{j\pi}{3}) && = 0,\\
&m = 1, n = 1, \quad \tfrac{1}{2} && \textstyle\sum_{j=1}^{6} \sin(2\varphi + \frac{2j\pi}{3}) && = 0,
\end{aligned}$$

and, for $m = 2, n = 0$ and $m = 0, n = 2$,

$$\begin{aligned}
\tfrac{1}{6h^2}\textstyle\sum_{j=1}^{6}(2h)^2 \cos^2(\varphi + \frac{j\pi}{3}) &= \tfrac{2}{3}\textstyle\sum_{j=1}^{6}\tfrac{1}{2}(1 + \cos(2\varphi + \frac{2j\pi}{3})) = 2,\\
\tfrac{1}{6h^2}\textstyle\sum_{j=1}^{6}(2h)^2 \sin^2(\varphi + \frac{j\pi}{3}) &= \tfrac{2}{3}\textstyle\sum_{j=1}^{6}\tfrac{1}{2}(1 - \cos(2\varphi + \frac{2j\pi}{3})) = 2.
\end{aligned}$$

This ends the proof. □

We turn to fourth-order method next.

4. Compact Schemes on Hexagons. Consider the Poisson equation in integral formulation $\frac{1}{|\Omega|}\iint_{\Omega}\triangle u \, dxdy = \frac{1}{|\Omega|}\iint_{\Omega} f \, dxdy$. We look for a (possible) compact scheme based on the configuration shown in Figs.2.1,4.1. Component triangles of the hexagon Ω are denoted by $\Omega_j \equiv \triangle P_0 V_j V_{j+1}$.

4.1. A naive compact scheme. With the centroid

$$M_j \equiv \frac{1}{3}(P_0 + V_j + V_{j+1}) \qquad \textit{and} \qquad \frac{\text{dist}(P_0, M_j)}{\text{dist}(P_j, M_j)} = \frac{1}{2},$$

a simple quadrature for domain integral on a hexagon can be derived as

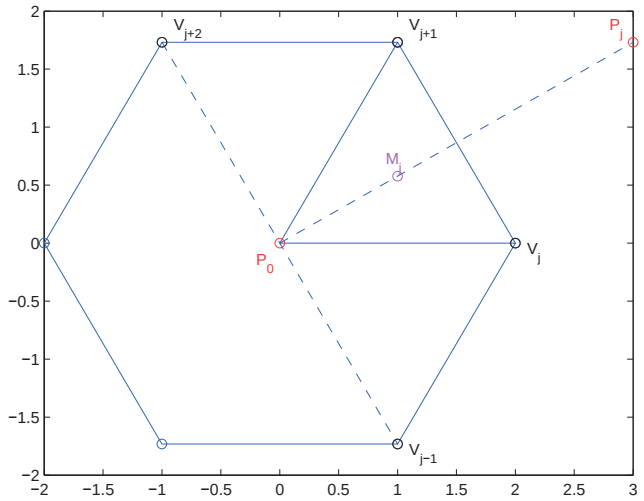

FIG. 4.1. *A simple quadrature for boundary integral on a hexagon.*

$$\begin{aligned}\tfrac{1}{|\Omega|}\int\!\!\int_{\Omega} f(x,y)dxdy &= \tfrac{1}{|\Omega|}\sum_{j=1}^{6}\int\!\!\int_{\Omega_j} f(x,y)dxdy \approx \tfrac{1}{|\Omega|}\sum_{j=1}^{6}\int\!\!\int_{\Omega_j} f(M_j)dxdy\\ &\approx \sum_{j=1}^{6}\tfrac{2f(P_0)+f(P_j)}{3}\tfrac{|\Omega_j|}{|\Omega|} = \tfrac{2}{3}f(P_0)+\tfrac{1}{18}\sum_{j=1}^{6}f(P_j)\ .\end{aligned}$$

This approximation to the definite integral is of second-order. Consequently, the associated compact scheme for the Poisson equation,

$$\begin{aligned}\tfrac{1}{h^2}\left(-u(P_0)+\tfrac{1}{6}\sum_{j=1}^{6}u(P_j)\right) &\approx \tfrac{1}{|\Omega|}\iint_{\Omega}\triangle u\,dxdy\\ &= \tfrac{1}{|\Omega|}\iint_{\Omega} f dxdy \approx \tfrac{2}{3}f(P_0)+\tfrac{1}{18}\sum_{j=1}^{6}f(P_j)\ ,\end{aligned}$$

is of second-order only.

4.2. A second hexagonal compact seven-point scheme. Based on Theorem A.1, it is natural to propose the following scheme

$$\begin{aligned}&\tfrac{1}{h^2}\left(-u(P_0)+\tfrac{1}{6}\sum_{j=1}^{6}u(P_j)\right)+\mathcal{O}(h^2) &&= \tfrac{1}{|\Omega|}\iint_{\Omega}\triangle u\,dxdy\\ =\ &\tfrac{1}{|\Omega|}\iint_{\Omega} f dxdy &&= f(P_0)+\tfrac{5}{36}h^2\triangle f+\mathcal{O}(h^4)\\ =\ & f(P_0)+\tfrac{5}{36}\left(-f(P_0)+\tfrac{1}{6}\sum_{j=1}^{6}f(P_j)+\mathcal{O}(h^4)\right)+\mathcal{O}(h^4)\\ =\ & \tfrac{31}{36}f(P_0)+\tfrac{5}{36}\left(\tfrac{1}{6}\sum_{j=1}^{6}f(P_j)\right)+\mathcal{O}(h^4)\ .\end{aligned}$$

We have analyzed this and it is not fourth-order. Because the right-hand side of the Poisson equation is replaced by the analytic fourth-order approximation, while the left-hand side is replaced by only a second-order scheme. The overall order of approximation to the Poisson equation is of second-order. Certainly, numerical experiments confirmed this.

4.3. Fourth-order hexagonal compact seven-point scheme. A third scheme reads

$$\frac{1}{h^2}\left(-u(P_0)+\frac{1}{6}\sum_{j=1}^{6}u(P_j)\right)=\frac{3}{4}f(P_0)+\frac{1}{24}\sum_{j=1}^{6}f(P_j)+\mathcal{O}(h^4),$$

which is Theorem A.3 restated for ease of comparison. We describe a different approach here. The stencil can be derived for hexagons with general phase angle by the method of undetermined coefficients. It is indeed fourth-order by construction below and also confirmed numerically. In the second compact scheme discussed in subsection 2, the stencil for the right-hand side is of fourth-order, but that for the left-hand side is not of as high order as required. To set up the stencil to achieve the highest possible order, we approximate the Poisson equation $\triangle u = u_{xx} + u_{yy} = f(x, y)$ by an algebraic linear seven-diagonal system

$$\sum_{j=0}^{6} A_j u(P_j) = \sum_{j=0}^{6} R_j f(P_j).$$

The fourteen coefficients $\{A_i{}'s, R_i{}'s\}$ are determined by imposing a normalization constraint

$$\textstyle\sum_{j=0}^{6} R_j = 1$$

and several interpolation conditions that the approximation be exact for some test functions, typically low degree monomials. Up to twenty-eight monomial test functions ($u(x, y) = x^m y^n,\ 0 \le m + n \le 6$) are considered as listed in Table 4.1. Several subsets of these are to be used.

TABLE 4.1
Shifted monomial test functions.

u	$f = \triangle u$	u	$f = \triangle u$	u	$f = \triangle u$
1	0	x^4	$12x^2$	x^6	$30x^4$
x	0	y^4	$12y^2$	y^6	$30y^4$
y	0	x^3y	$6xy$	x^5y	$20x^3y$
x^2	2	xy^3	$6xy$	xy^5	$20xy^3$
y^2	2	x^2y^2	$2x^2 + 2y^2$	x^4y^2	$2x^4 + 12x^2y^2$
xy	0	x^5	$20x^3$	x^2y^4	$12x^2y^2 + 2y^4$
x^3	$6x$	y^5	$20y^3$	x^3y^3	$6xy^3 + 6x^3y$
y^3	$6y$	x^4y	$12x^2y$		
x^2y	$2y$	xy^4	$12xy^2$		
xy^2	$2x$	x^3y^2	$2x^3 + 6xy^2$		
		x^2y^3	$6x^2y + 2y^3$		

In this framework, the stencils for the three schemes discussed in current section are, $R =$

$$\left(\tfrac{12.0}{18}, \tfrac{1}{18}, \tfrac{1}{18}, \tfrac{1}{18}, \tfrac{1}{18}, \tfrac{1}{18}, \tfrac{1}{18}\right), \left(\tfrac{15.5}{18}, \tfrac{5}{216}, \tfrac{5}{216}, \tfrac{5}{216}, \tfrac{5}{216}, \tfrac{5}{216}, \tfrac{5}{216}\right), \left(\tfrac{13.5}{18}, \tfrac{1}{24}, \tfrac{1}{24}, \tfrac{1}{24}, \tfrac{1}{24}, \tfrac{1}{24}, \tfrac{1}{24}\right),$$

respectively, and

$$A = \tfrac{1}{h^2}\left(-1, \tfrac{1}{6}, \tfrac{1}{6}, \tfrac{1}{6}, \tfrac{1}{6}, \tfrac{1}{6}, \tfrac{1}{6}\right).$$

The third scheme is exact at least for monomials $\{x^m y^n \mid 0 \le m + n \le 6\}$, except for $\{x^6, y^6, x^4y^2, x^2y^4\}$. Notably, the 13 monomials best-chosen as test functions differed between configurations type I and II in a numerical approach.

4.4. Net of three-color finite volumes. To accelerate the convergence in an iterative procedure, we propose

ALGORITHM 1. *(Three-color algorithm.) With* $i, j = 1, 2, \cdots$ *, we define color* $\in \{0, 1, 2\}$ *at each FV (center) of a cartesian net of type I or II hexagons (Fig.2.1), respectively, by*

$$color = \mod\big(\, j + 1 - 2 \cdot \mod(i, 2),\ 3\,\big),$$

or

$$color = \mod\big(\, i + 1 - 2 \cdot \mod(j, 2),\ 3\,\big).$$

In C-language, the expressions are

$$\big(j + 1 - 2 * (i\%2)\big)\%3\,, \quad \textit{and} \quad \big(i + 1 - 2 * (j\%2)\big)\%3\,.$$

We assign three colors to hexagonal FVs and make use even in a time march procedure. Plain Jacobi type explicit forward Euler schemes are usually adopted for time-dependent problems. However, we can rearrange the order of updates at hexagonal centers. The same idea certainly applies to cartesian quadrangle type FVs. This is further investigated in subsection 5.3.

REMARK 1. *The three-color ordering update on a net of hexagonal FVs is applicable in a parallel fashion. The model of parallel computation better be SPMD (single-program-multiple-data) with shared memory. We note, without giving the algorithmic detail, that part of the computation in a time march demands for synchronous (Jacobi) update while the others need asynchronous (GS) update for faster convergence. The multicolor update algorithm may help in this respect.*

4.5. Solving time-dependent problems. We consider for simplicity the linear diffusion equation $u_t = D(u_{xx} + u_{yy})$ with constant diffusivity. Proper initial and boundary conditions are assumed. In application of a standard time-marching procedure with h_t denoting the temporal stepsize, we note the followings ([6]).

1. *Second-Order Implicit Scheme.*

$$\frac{u_{P_0}^{n+1} - u_{P_0}^{n}}{h_t} = \frac{D}{h^2}\left(-u_{P_0}^{n+1} + \frac{1}{6}\sum_{i=1}^{6} u_{P_i}^{n+1}\right). \tag{4.1}$$

2. *Fourth-Order Fully-Implicit Scheme.*

$$\frac{3}{4}\frac{u_{P_0}^{n+1} - u_{P_0}^{n}}{h_t} + \frac{1}{24}\sum_{i=1}^{6}\frac{u_{P_i}^{n+1} - u_{P_i}^{n}}{h_t} = \frac{D}{h^2}\left(-u_{P_0}^{n+1} + \frac{1}{6}\sum_{i=1}^{6} u_{P_i}^{n+1}\right). \tag{4.2}$$

These schemes are tested next.

5. Numerical Experiments and Discussions. Test runs are conducted on both static and time-dependent problems.

5.1. Seven-point methods on elliptic equations. Poisson and Helmholtz equations are tested on square regions.

1. *A Poisson equation.* This is similar to model problem G from *Ellpack* [9], but here with a slightly more singular solution $u(x, y) = (xy)^{2.1}$ on domain $[1, 2]^2$. As shown in Table 5.1, the H7 and H7c schemes (4.1,4.2) are of second and fourth-order respectively, and the three-color (*3c-gs*) hexagonal FVM is indeed effective. The *Ratio* column in the table refers to the discrete normalized *2-norm* of errors at FV centers. The *3c-gs* update algorithm achieved the same accuracy as *Jac* and *GS* methods in about half many iterations as the *Jac* method. Indeed, even in *sequential* computation the iteration count of *3c-gs* is slightly fewer than that of the *GS* method.

TABLE 5.1

Seven-point methods with three-color vs Jacobi and Gauss-Seidel iterations on Poisson equation, using $tol_x = 1.0e-14$ *and* $tol_f = 1.0e-15$ *for Cauchy convergence and residual check.*

$Method$	$Gridsize$	Err_{max}	Err_2	$Ratio$	$Iter_{Jac}$	$Iter_{GS}$	$Iter_{3c-gs}$
H7	15x15	3.5548e-04	2.1054e-04		1346	691	689
H7	30x30	8.7683e-05	5.0565e-05	4.16	4881	2506	2501
H7	60x60	2.1797e-05	1.2383e-05	4.08	18123	9299	9286
H7c	15x15	1.7353e-08	1.0608e-08		1345	691	689
H7c	30x30	1.0930e-09	6.4749e-10	16.39	4880	2504	2499
H7c	60x60	6.2416e-11	3.6847e-11	17.57	18122	9299	9287

TABLE 5.2

Seven-point method with three-color vs Jacobi and Gauss-Seidel iterations on Helmholtz equation, using $tol_x = 1.0e-15$ *and* $tol_f = 1.0e-18$ *for Cauchy convergence and residual check.*

$Method$	$Gridsize$	Err_{max}	Err_2	$Ratio$	$Iter_{Jac}$	$Iter_{GS}$	$Iter_{3c-gs}$
H7	15x15	4.7586e-03	1.8958e-03		231	125	120
H7	30x30	9.3584e-04	3.7005e-04	5.12	839	440	432
H7	60x60	2.0649e-04	8.1292e-05	4.55	3135	1626	1610

2. *A Helmholtz equation.* The hexagonal seven-point scheme (H7) is also effective on Helmholtz equations (model problem C from *Ellpack* on $[0,1]^2$). Results shown in Table 5.2 justifies this. The compact H7c stencil, as stated in Section 4.3, does not yield fourth-order convergence in the Helmholtz equation. The weights need to be modified depending on each application, particularly in case of variable coefficients in a time march problem.

5.2. Monodomain model of electrical wave propagation in cardiac tissue. To simulate electrical activation of cardiac tissue, there are two available models, bidomain and monodomain models. The bidomain equations[12] consist of an elliptic partial differential equation and a parabolic differential equation, coupled with a system of nonlinear ordinary differential equations for ionic dynamics. Although bidomain model can provide more information such as anisotropy effect of tissue conductivity, solving bidomain equations is computationally expensive [16]. The system of bidomain equations is reduced to monodomain equations as a reaction-diffusion (R-D) system, under the assumption of equal anisotropies. For electrical wave propagation, differences between bidomain and monodomain equations are relatively small [8]. The system of monodomain equations is numerically efficient and accepted by many in studying electrical wave propagation of cardiac tissue [1, 11, 13].

The monodomain equation reads

$$\frac{\partial u}{\partial t} = \nabla(\boldsymbol{M}\nabla u) - I_{ion}(t, u(t,x,y)) - I_{stim}(t,x,y),$$

where I_{ion} is the ionic currents through cell membrane and I_{stim} represents stimulation current given to the cell. In this work, the human ventricular cell model developed by ten Tusscher et.al.[14] is used to simulate the ionic activity and action potential of myocardium. Both linear and spiral wave phenomena are studied using explicit forward Euler time march. For all test runs, computational domains consist of quadrangle (*Quad*) or hexagonal (*Hexa*) FVs. Twenty-five tracers are deployed. The calculated values of the primitive variable u are recorded at these tracers at various times. We discuss the details next.

5.3. Three-color ordering update in time march.. To investigate linear wave propagation in cardiac tissue in an approximated square region, a uni-direction linear wave started

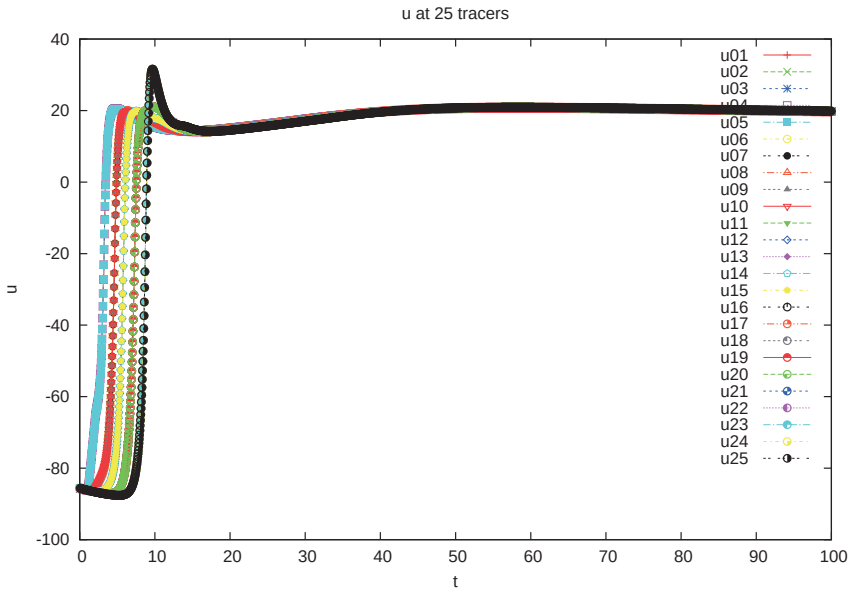

FIG. 5.1. *A stable linear wave.*

initially at the left edge of the region, caused by electrical stimulation at the whole edge in a short time frame. Tests are using *Quad* FVs or type I,II *Hexa* FVs approximating the square region, with computation on boundary-fitted cell-centered FVs. Simulation time is up to *100* or *1000*. Time plots of the dependent variables at twenty-five tracers are shown in Figs. 5.1, 5.2 using *Hexa* I FVs. These figures indicate clearly a linear wave solution, which is well-developed after some time. We note the time span needs to be as large as about 500 for a full cycle of the wave. Visually identical results were obtained using *Hexa* II and *Quad* FVs.

Numerical data are collected in Table 5.3. Explicit forward Euler method is applied in a time march procedure. This corresponds to a regular (natural order) Jacobi type update. Symmetric multicolor ordering updates are also adopted for comparison. In the *Quad* FV case, the update order is *odd-even* at odd time steps and *even-odd* at even time steps, so as to be fair in operation complexity. when compared with regular Jacobi update. Similar simple design is adopted in *three-color* update on *Hexa* FVs, i.e., forward or backward in the ordered colors alternatingly in all time steps. We note this is not a full symmetric version. Wave speeds $s(2:5, 2:5)$ are measured using twenty-five tracers, with speeds $s(i = 5, j = 1:5)$ shown in the table. Based on the results of Quad method as benchmark values, relative ratios (last column in table) are calculated, separately, for the Jacobi iterations and the multi-color ones. The physics being a travelling wave towards the right, the *Quad* FVs are certainly best suited. Results of the *Hexa II* FVs are close within *0.5%* in Jacobi update, and within *0.2%* in three-color update. We recall the Type I and II *Hexa* FVs, with phase angle $\varphi = 0, -\pi/6$ respectively, are the two extremes of all possible configurations of hexagons (Fig.2.1). The corresponding computational results in the table shows a *5.4%* deviation between these two extremes. With multicolor update algorithms, the deviation is *6.7%*. We conclude that, (even) on a square domain, the computational results using hexagonal FVs are not very different from using rectangular (Quad) FV, while hexagonal FVM can be applied in general appli-

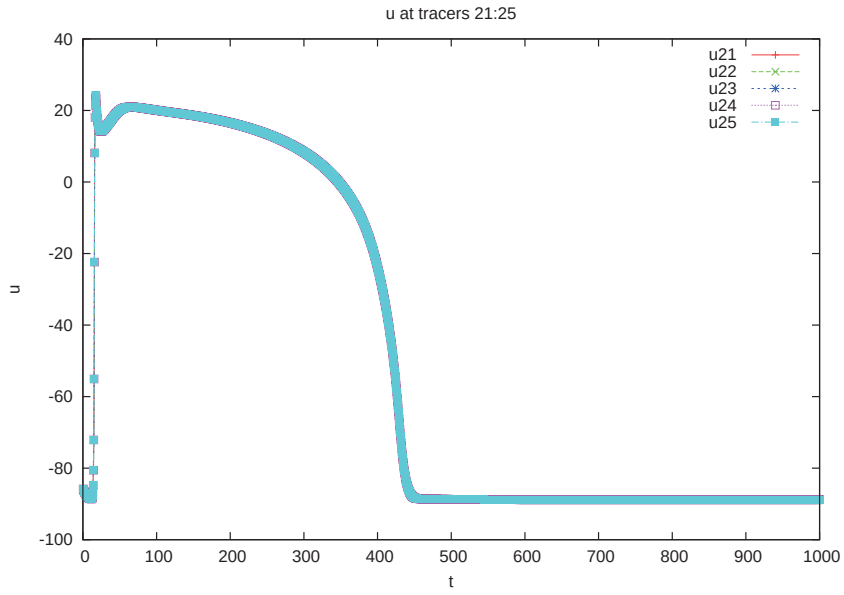

FIG. 5.2. *Action potential for human ventricular M-cells.*

TABLE 5.3
Wave speeds using symmetric multicolor GS vs Jacobi updates in time march.

FV	$Euler\ method$	$s(5,1)$	$s(5,2)$	$s(5,3)$	$s(5,4)$	$s(5,5)$	$Speed_{av}$	$Ratio$
Quad	Jocobi	0.556	0.556	0.556	0.556	0.556	0.556	1.000
Quad	symm BW-order	0.579	0.579	0.579	0.579	0.579	0.579	1.000
Hexa II	Jocobi	0.550	0.553	0.553	0.550	0.568	0.553	0.995
Hexa II	symm 3-color	0.572	0.577	0.577	0.573	0.591	0.578	0.998
Hexa I	Jocobi	0.510	0.524	0.527	0.527	0.529	0.523	0.941
Hexa I	symm 3-color	0.527	0.540	0.543	0.541	0.544	0.539	0.931

cation that may exhibit various kinds of wave phenomena, especially in curved regions [6].

We mention that spiral wave can be generated as shown in Fig.5.3. Linear wave started initially as in the previous group of tests, it was then followed in a later time by a second stimulation at the first half of the top edge, resulting in a self-sustained spiral wave. It is noticed the contours turn from vertical to circular after the second stimulation. The simulation time is up to *500* using *Hexa II* FVs.

6. Conclusions. Both ordinary and compact hexagonal seven-point stencils of two-dimensional discrete laplacian are investigated in a finite volume approach. A three-color algorithm is developed for use in an iterative update procedure. This is confirmed effective in elliptic problems and also in a time march procedure. Using hexagonal finite volumes, linear and spiral waves in a square-like region are exhibited successfully based on the monodomain model. The application to wide range of numerical heart modeling is potentially of great value. We think this applies in many applications in two-dimensional irregular regions.

Acknowledgments. The authors are grateful to Tunghai university and Providence university for continued laboratory support for a long period of time.

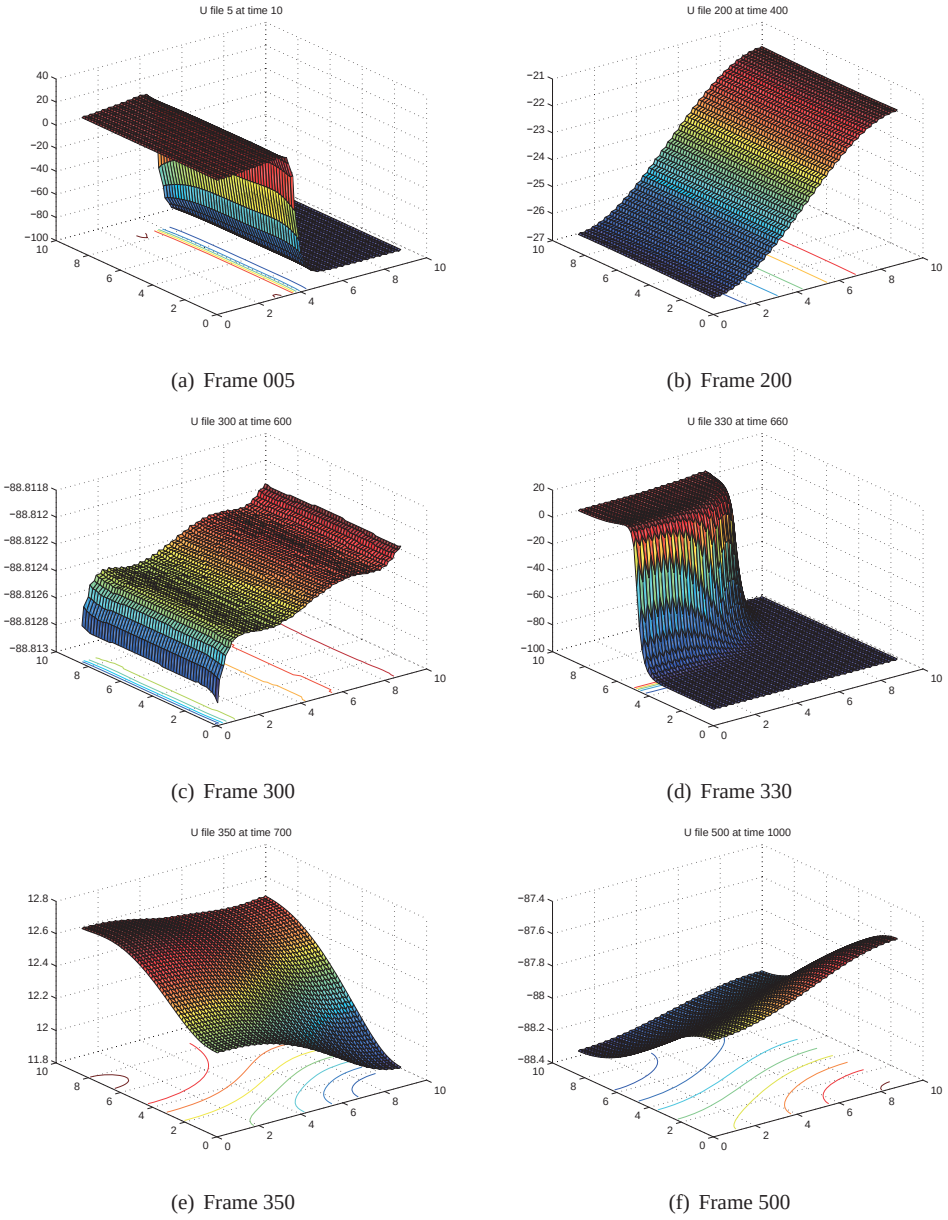

(a) Frame 005 (b) Frame 200

(c) Frame 300 (d) Frame 330

(e) Frame 350 (f) Frame 500

FIG. 5.3. *Surface and contour plots of a spiral wave. The contours turn circular after the second stimulation.*

REFERENCES

[1] R.R. ALIEV AND A.V. PANFILOV, A simple two-variables model of cardiac excitation, *Chaos, Solitons and Fractals*, **7**:3 (1996), pp. 293-301.

[2] RITSEMA VAN ECK HJ, J.A. KORS AND G. VAN HERPEN, The U wave in the electrocardiogram: a solution for a 100-year-old riddle. *Cardiovasc Res.*, **67**:2 (2005), pp. 256-262.

[3] B. HE, *Modeling and Imaging of Bio-electrical Activity: Principle and Applications*, Kluwer Academic/Plenum Publishers, New York 2004.

[4] D. LEE, A new approach to finite-volume-finite-difference methods, *Chinese Journal of Numerical Math-*

ematics and Applications, **21**:2 (1999), pp. 96-102.
[5] D. LEE AND M. YU, On an improved finite-volume-difference method in fluids computation, *Transaction of the Aeronautical Society of the Republic of China*, **33**:3 (2001), pp. 171-179.
[6] D. LEE, H.C. TIEN, C.P. LUO AND H.-N. LUK, Hexagonal grid methods with applications to partial differential equations. (*In preparation.*)
[7] W.M. PICKERING, On the solution of Poisson's equation on a regular hexagonal grid Using FFT Methods. *JCP*, **64** (1986), pp. 320-333.
[8] M. POSTSE, B. DUBE, J. RICHER, A. VINET AND R.M. GULRAJANI, A comparison of monodomain and bidomain reaction-diffusion models for action potential propagation in the human heart, *IEEE Transaction on Biomedical Engineering*, **53**:12 (2006), pp. 2425-2435.
[9] J.R. RICE AND R.F. BOISVERT, *Solving Elliptic Problems with ELLPACK*. Springer-Verlag, 1985.
[10] J.B. ROSER, Nine point difference solutions for Poisson's equation, *Comp. Math. Appl.*, **1** (1975), pp. 351-360.
[11] H. SAKAGUCHI AND T. FUJIMOTO, Elimination of spiral chaos by periodic force for the Aliev-Panfilov model. *Phys. Rev. E*, **71** (2005) 052901.
[12] L. TUNG, *A bi-domain model for describing ischemic myocardial D-C potentials*, PhD thesis, MIT Cambridge, MA 1978.
[13] K.H.W.J. TEN TUSSCHER AND A.V. PANFILOV, Wave propagation in excitable media with randomly distributed obstacles, *Multiscale model simulation*, **3**:2 (2005), pp. 265-282.
[14] K.H.W.J.TEN TUSSCHER AND A.V.PANFILOV, Alternans and spiral breakup in a human ventricular tissue model, *Am J Physiol Heart Circ Physiol 291:H1088-H1100,2006.*
[15] H.K. VERSTEEG AND W. MALALASEKERA, *An Introduction to Computational Fluid Dynamics, the Finite Volume Method.*, Longman Group Ltd 1995.
[16] E.J. VIGMOND, R.W.D. SANTOS, A.J. PRASSL, M. DEOCW AND G. PLANK, Solvers for the cardiac bidomain equations, *Progress in Biophysics and Molecular Biology*, 96 (2008), pp. 3-18.

Appendix A. Functional Approximations in a Hexagon. Assume Ω is a regular hexagon in general configuration with phase angle φ and centered at $P_0 = (x_0, y_0)$. We denote the radius by r, and the height by $h(= \frac{\sqrt{3}}{2}r)$. The six neighbor (center) nodes are (Fig.4.1) $P_j := V_j + V_{j+1} - P_0$. Precisely,

$$P_j := (x_j, y_j) = (x_0, y_0) + 2h(\cos\theta_j, \sin\theta_j), \quad \text{with } \theta_j = \varphi - \frac{\pi}{6} + \frac{j\pi}{3}, \ \ j = 1, \cdots, 6\ .$$

Let $f(x, y)$ be a smooth function defined in Ω. The followings were obtained by the authors.

THEOREM A.1. *The expression,*

$$\begin{aligned} \frac{1}{|\Omega|}\int\int_{\Omega} f(x,y)dxdy &= f(P_0) + \tfrac{5}{48}r^2\triangle f + \mathcal{O}(r^4) \\ &= f(P_0) + \tfrac{5}{36}h^2\triangle f + \mathcal{O}(h^4), \end{aligned} \tag{A.1}$$

is valid and implies a fourth-order analytic approximation to the definite integral of a smooth integrand over a regular hexagon, in terms of values of the function and its laplacian at center of the hexagon.

We note similar result is available on rectangles ([4],[5]).

In application to differential equations, we consider Poisson equation in its simplest form, $\triangle u = u_{xx} + u_{yy} = f(x, y)$.

THEOREM A.2. *The differential relation,*

$$u_{xx}(x_0, y_0) + u_{yy}(x_0, y_0) = f(x_0, y_0),$$

is approximated by the discrete hexagonal ordinary seven-point (H7) scheme,

$$\frac{1}{h^2}\left(-u(x_0, y_0) + \frac{1}{6}\sum_{j=1}^{6} u(x_j, y_j)\right) = f(x_0, y_0)\ ,$$

which is second-order accurate, that is,

$$\begin{aligned} u_{xx}+u_{yy} &= \tfrac{1}{h^2}\left(-u(P_0)+\tfrac{1}{6}\textstyle\sum_{i=1}^{6}u(P_i)\right)-\tfrac{h^2}{4}(u_{xxxx}+2u_{xxyy}+u_{yyyy})+\mathcal{O}(h^4) \\ &= \tfrac{1}{h^2}\left(-u(P_0)+\tfrac{1}{6}\textstyle\sum_{i=1}^{6}u(P_i)\right)+\mathcal{O}(h^2). \end{aligned} \tag{A.2}$$

Furthermore is true.

THEOREM A.3. *(Fourth-order hexagonal compact seven-point (H7c) scheme.)*

$$\frac{1}{h^2}\left(-u(P_0)+\frac{1}{6}\sum_{i=1}^{6}u(P_i)\right)=\frac{3}{4}f(P_0)+\frac{1}{24}\sum_{i=1}^{6}f(P_i)+\mathcal{O}(h^4). \tag{A.3}$$

We refer to [10] for a fourth-order compact scheme on rectangles.

We note that, the above result (A.3) for the special case of type II hexagons, embedded in a mesh of triangles, was used in [7] without an explicit proof. The result in its most general form is given in [6]. We prove the result for the special case of a type II hexagon in the next section.

Appendix B. Finite difference method : type II hexagons. We derive Eq.(A.3) for regular type II hexagons using conventional FD notations. We recall the center-to-center distance $d=2h=\sqrt{3}r$.

Consider the center and six neighbor nodes of a type II hexagon,

$$P_0=(0,0),\quad P_j=d\,(\cos(j\pi/3),\ \sin(j\pi/3))\,,\quad 1\le j\le 6.$$

We denote for convenience that

$$\begin{aligned} &P_{NE}=P_1=(\tfrac{d}{2},\tfrac{\sqrt{3}d}{2}), && P_{NW}=P_2=(\tfrac{-d}{2},\tfrac{\sqrt{3}d}{2}), && P_W=P_3=(-d,0),\\ &P_{SW}=P_4=(\tfrac{-d}{2},\tfrac{-\sqrt{3}d}{2}), && P_{SE}=P_5=(\tfrac{d}{2},\tfrac{-\sqrt{3}d}{2}), && P_E=P_6=(d,0). \end{aligned}$$

The associated values of a function $u(x,y)$ are denoted by

$$u_P,\quad u_{NE},\quad u_{NW},\quad u_W,\quad u_{SW},\quad u_{SE},\quad u_E,$$

at the center and neighbor nodes, respectively. Assuming appropriate smoothness of the function u, truncated Taylor expansions yield the following

$$\begin{aligned} u_E &\approx u_P+du_x+\tfrac{d^2}{2}u_{xx}+\tfrac{d^3}{6}u_{xxx}+\tfrac{d^4}{24}u_{xxxx}+\tfrac{d^5}{120}u_{xxxxx}\,,\\ u_W &\approx u_P-du_x+\tfrac{d^2}{2}u_{xx}-\tfrac{d^3}{6}u_{xxx}+\tfrac{d^4}{24}u_{xxxx}-\tfrac{d^5}{120}u_{xxxxx}, \end{aligned}$$

$$\begin{aligned} u_{NE}\approx u_P &+ \tfrac{d}{2}u_x+\tfrac{\sqrt{3}d}{2}u_y+\tfrac{d^2}{2}\left(\tfrac{1}{4}u_{xx}+2\cdot\tfrac{\sqrt{3}}{4}u_{xy}+\tfrac{3}{4}u_{yy}\right)\\ &+ \tfrac{d^3}{6}\left(\tfrac{1}{8}u_{xxx}+3\cdot\tfrac{\sqrt{3}}{8}u_{xxy}+3\cdot\tfrac{3}{8}u_{xyy}+\tfrac{3\sqrt{3}}{8}u_{yyy}\right)\\ &+ \tfrac{d^4}{24}\left(\tfrac{1}{16}u_{xxxx}+4\cdot\tfrac{\sqrt{3}}{16}u_{xxxy}+6\cdot\tfrac{3}{16}u_{xxyy}+4\cdot\tfrac{3\sqrt{3}}{16}u_{xyyy}+\tfrac{9}{16}u_{yyyy}\right),\\ u_{SE}\approx u_P &+ \tfrac{d}{2}u_x-\tfrac{\sqrt{3}d}{2}u_y+\tfrac{d^2}{2}\left(\tfrac{1}{4}u_{xx}-2\cdot\tfrac{\sqrt{3}}{4}u_{xy}+\tfrac{3}{4}u_{yy}\right)\\ &+ \tfrac{d^3}{6}\left(\tfrac{1}{8}u_{xxx}-3\cdot\tfrac{\sqrt{3}}{8}u_{xxy}+3\cdot\tfrac{3}{8}u_{xyy}-\tfrac{3\sqrt{3}}{8}u_{yyy}\right)\\ &+ \tfrac{d^4}{24}\left(\tfrac{1}{16}u_{xxxx}-4\cdot\tfrac{\sqrt{3}}{16}u_{xxxy}+6\cdot\tfrac{3}{16}u_{xxyy}-4\cdot\tfrac{3\sqrt{3}}{16}u_{xyyy}+\tfrac{9}{16}u_{yyyy}\right),\\ u_{NW}\approx u_P &- \tfrac{d}{2}u_x+\tfrac{\sqrt{3}d}{2}u_y+\tfrac{d^2}{2}\left(\tfrac{1}{4}u_{xx}-2\cdot\tfrac{\sqrt{3}}{4}u_{xy}+\tfrac{3}{4}u_{yy}\right)\\ &+ \tfrac{d^3}{6}\left(\tfrac{1}{8}u_{xxx}+3\cdot\tfrac{\sqrt{3}}{8}u_{xxy}-3\cdot\tfrac{3}{8}u_{xyy}+\tfrac{3\sqrt{3}}{8}u_{yyy}\right)\\ &+ \tfrac{d^4}{24}\left(\tfrac{1}{16}u_{xxxx}-4\cdot\tfrac{\sqrt{3}}{16}u_{xxxy}+6\cdot\tfrac{3}{16}u_{xxyy}-4\cdot\tfrac{3\sqrt{3}}{16}u_{xyyy}+\tfrac{9}{16}u_{yyyy}\right),\\ u_{SW}\approx u_P &- \tfrac{d}{2}u_x-\tfrac{\sqrt{3}d}{2}u_y+\tfrac{d^2}{2}\left(\tfrac{1}{4}u_{xx}+2\cdot\tfrac{\sqrt{3}}{4}u_{xy}+\tfrac{3}{4}u_{yy}\right)\\ &+ \tfrac{d^3}{6}\left(-\tfrac{1}{8}u_{xxx}-3\cdot\tfrac{\sqrt{3}}{8}u_{xxy}-3\cdot\tfrac{3}{8}u_{xyy}-\tfrac{3\sqrt{3}}{8}u_{yyy}\right)\\ &+ \tfrac{d^4}{24}\left(\tfrac{1}{16}u_{xxxx}+4\cdot\tfrac{\sqrt{3}}{16}u_{xxxy}+6\cdot\tfrac{3}{16}u_{xxyy}+4\cdot\tfrac{3\sqrt{3}}{16}u_{xyyy}+\tfrac{9}{16}u_{yyyy}\right), \end{aligned}$$

$$\begin{aligned} u_{NE}+u_{SE} &\approx 2u_P+2\left(\tfrac{d}{2}u_x+\tfrac{d^2}{2}(\tfrac{1}{4}u_{xx}+\tfrac{3}{4}u_{yy})+\tfrac{d^3}{6}(\tfrac{1}{8}u_{xxx}+\tfrac{9}{8}u_{xyy})\right.\\ &\quad \left.+\tfrac{d^4}{24}(\tfrac{1}{16}u_{xxxx}+\tfrac{18}{16}u_{xxyy}+\tfrac{9}{16}u_{yyyy})\right),\\ u_{NW}+u_{SW} &\approx 2u_P+2\left(\tfrac{-d}{2}u_x+\tfrac{d^2}{2}(\tfrac{1}{4}u_{xx}+\tfrac{3}{4}u_{yy})-\tfrac{d^3}{6}(\tfrac{1}{8}u_{xxx}+\tfrac{9}{8}u_{xyy})\right.\\ &\quad \left.+\tfrac{d^4}{24}(\tfrac{1}{16}u_{xxxx}+\tfrac{18}{16}u_{xxyy}+\tfrac{9}{16}u_{yyyy})\right). \end{aligned}$$

Therefore,

$$u_E+u_W-2u_P=d^2u_{xx}+\tfrac{d^4}{12}u_{xxxx}+\mathcal{O}(d^6)$$

and

$$u_{NE}+u_{NW}+u_{SE}+u_{SW}-4u_P=d^2\left(\frac{1}{2}u_{xx}+\frac{3}{2}u_{yy}\right)+d^4\left(\frac{1}{96}u_{xxxx}+\frac{18}{96}u_{xxyy}+\frac{9}{96}u_{yyyy}\right)+\mathcal{O}(d^6).$$

Adding the last two equations, we obtain a second-order seven-point scheme for the laplacian with an error estimate,

$$\begin{aligned} &\frac{u_{NE}+u_{NW}+u_{SE}+u_{SW}+u_E+u_W-6u_P}{\frac{3}{2}d^2}\\ =&u_{xx}+u_{yy}+\frac{d^2}{16}(u_{xxxx}+2u_{xxyy}+u_{yyyy})+\mathcal{O}(d^4). \end{aligned} \tag{B.1}$$

This ends proving Eq.(A.3) for the special case that phase angle $\varphi=-\pi/6$. □

三色六角形有限體積方法於心臟生理之模擬計算

李天佑　　田慧君

摘 要

本文發展網式六角形有限體積之三色迭代更新算法，用於解決定常拉氏方程佳可必更新法之平行化。並用於時步法之三色非同步更新，效益明顯。

模擬計算包括：(1)橢圓形方程之標準測試，由數值結果可知 2 種網式六角形有限體積之三色迭代更新算法分別可達 2 階及 4 階之精準。(2)應用於模擬人類心室細胞組織之電生理活動。可得到精確之心室細胞動作電位及細胞組織之間動作電位傳遞形式之直行波，螺旋波亦可實現。